Received: 15 February 2021 | Revised: 22 May 2021 | Accepted: 7 June 2021

IET Microwaves, Antennas & Propagation

DOI: 10.1049/mia2.12168

The Institution of Engineering and Technology WILEY

ORIGINAL RESEARCH PAPER

Analysis and modelling of rampart line antennas

Giulia Sacco[1,2] | Olivier Caytan[3] | Stefano Pisa[1] | Hubregt J. Visser[2,4]

[1]Department of Information Engineering, Electronics and Telecommunication of Sapienza University of Rome, Rome, Italy

[2]Stichting IMEC Netherlands, Eindhoven, Netherlands

[3]IDLab, Department of Information Technology, Ghent University—IMEC, Ghent, Belgium

[4]Department of Electrical Engineering, Electromagnetics Group, Eindhoven University of Technology, The Netherlands

Correspondence

Giulia Sacco, Department of Information Engineering, Electronics and Telecommunication of Sapienza University of Rome, 00184 Rome, Italy.
Email: giulia.sacco@uniroma1.it

Abstract

A new, efficient, and accurate analytical model is introduced for estimating the beam direction of rampart line antennas with microstrip radiators that can change beam direction with feeding frequency. The model takes its origins from 1-D array theory, in which the bends represent the radiating elements, and the interconnecting lines represent the phase shifters. A mathematical expression accounting for the equivalent length of the bends for the correct estimation of the distance between the radiators is introduced. The model was tested for various substrate relative permittivity values ranging from 2.9 to 6.45. This model can be used for arbitrary rampart line configurations by providing the equivalent dipole direction, depending on the orientation of the bends. An alternative geometry was proposed to reduce the coupling between the parallel line segments. A prototype operating in a bandwidth of 1 GHz around 7.8 GHz was realized on a Rogers RO4350B high-frequency laminate with a thickness of 1.524 mm. Both the radiation pattern and the reflection coefficient were measured and show a good agreement with the proposed analytical model and commercial full-wave simulation tool results.

1 | INTRODUCTION

Frequency scanning antennas are commonly used for wideband applications that require the investigation of directions different from the broadside. Typical examples are ultra-wideband (UWB) radars that can employ these antennas to perform two-dimensional localization by providing range and azimuth information [1–6]. Compared with multiple-input multiple-output (MIMO) systems that have also been used for this application [7–9], the main advantage is that only two radiators are required, one for the transmission and one for the reception. Indeed, MIMO radars require an array of antennas, and consequently, multiple transmitters and receivers. These additional components cause higher power consumption, need complex and lossy feeding networks, and require a higher amount of data to be processed. In addition, with MIMO radar, the information along one specific direction is reconstructed by combining signals collected by low-gain omnidirectional radiating sources. This reconstruction approach is in contrast to frequency scanning antennas with which only one direction at a time is investigated by the electromagnetic radiation with a high gain beam, thus minimizing the influence of other targets or static reflectors located in neighbouring directions. The classic frequency scanning linear array antenna is the slotted waveguide array antenna, initially proposed in [10] and more recently revisited in [11–17]. The main drawback of this kind of antenna is its bulkiness, a characteristic that is not always acceptable. For this reason, printed antennas, thanks to their smaller dimension, are a preferable solution. However, resonant printed antenna elements seem unsuitable because they inherently have an extremely narrow frequency bandwidth.

In [18–21], the rampart line antenna, a frequency scanning printed antenna, is proposed. This radiator is a travelling wave antenna realized with a meandered microstrip line that guarantees a wide band and reduced complexity. The antenna has been revised more recently in [22, 23]. Various models have been developed over the years for this antenna topology [19, 24–27]. In [19], the antenna is treated as a 1-D array of radiating elements, but this model is formulated only for the geometry described in the work and does not consider the effective length of the microstrip bends. In [24], empirical relations for the design of this radiator topology are proposed. In [25], a transmission line model for travelling wave antennas with right-angled bends is presented. This approach yields accurate results but is limited mainly to configurations with right-angle bends and requires complex analysis to obtain the far-field information. In [26], a circuital model of the unit cell is presented.

In addition, in this case the model is made for a rampart line antenna with right-angle bends and requires quite complicated and computationally expensive preanalysis work. In [27], a method of moments approach for analysing lossless right-angle rampart line antennas is proposed. This solution, even if accurate, is computationally expensive. In the cited references, rampart line antennas are designed using hardware or software experiments [20, 22], applying phased array antenna (PAA) theory [18, 19, 21, 22, 25], or applying leaky-wave antenna (LWA) theory [26, 28, 29]. Both theoretical approaches are valid. Here, we have chosen to adopt the PAA design approach, as in [18, 19], where we aim for an analytical model that is easy to implement in software and is easy to use. The model will be used to generate an initial design that is fine-tuned through the use of full-wave electromagnetic analysis software.

In this work, an efficient and accurate model based on 1-D array theory [30] is proposed. Contrary to previous models, fundamental aspects are modelled that are challenging to retrieve, such as the effective length of the corners, thus guaranteeing precise prediction of the main beam pointing direction. Model accuracy is assessed by comparing the obtained results with those resulting from full-wave electromagnetic analysis. Furthermore, a modified geometry of the rampart line antenna is proposed to reduce the coupling between parallel microstrip lines. An antenna operating in the bandwidth ranging from 7.3 to 8.3 GHz is designed with the proposed geometry, and a prototype is realized. Both the reflection coefficient and the radiation pattern at multiple frequency values inside the bandwidth have been measured. They are in good agreement with full-wave simulation results. The proposed model accurately estimates the main beam pointing direction for the realized prototype, showing a maximum error of about 2.8° for a 3 dB beamwidth of 16.9°.

The rampart line antenna radiation mechanism and the geometric parameter influences on the far-field are presented in Section 2 together with the traditional and modified geometry. Section 3 reports the model formulation, which is first derived for the traditional geometry and then extended to the newly proposed one. In Section 4, simulation results are shown. Section 5 reports the measurements and compares the proposed model and the simulations for the realized prototype. In Section 6, conclusions are drawn. In Section 7, the LWA theory used to describe this kind of antenna is presented and is compared with the proposed model.

2 | ANTENNA CONFIGURATIONS AND RADIATION MECHANISM

Rampart line antennas are microstrip travelling wave radiators realized by the periodic repetition of a printed block wave structure formed by sections of microstrip transmission lines interconnected with chamfered corners. The antenna is fed from one of its extremities and terminated by a matched load at the other one. The characteristics of the antenna can be modified in terms of area occupancy, coupling between parallel microstrip segments, and antenna polarization by changing the number of

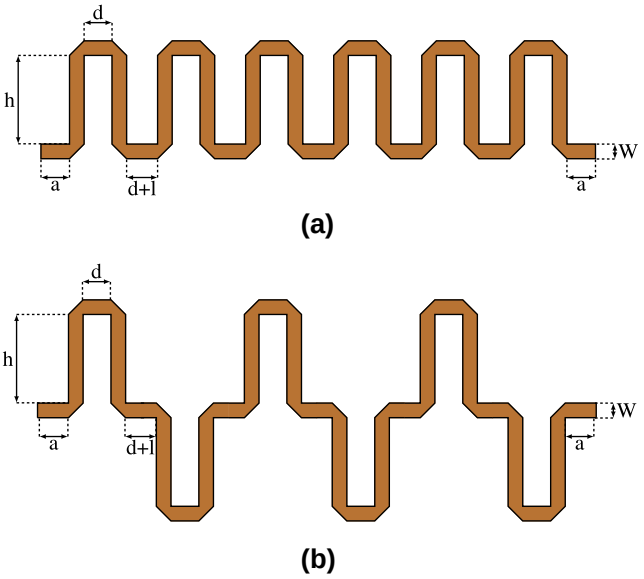

FIGURE 1 Rampart line antenna: (a) traditional geometry [18] (b) proposed geometry with half the periods flipped

corners per period and their physical disposition. In this work, the geometry described in [18] (Figure 1a) is analysed along with a new one (Figure 1b) obtained by flipping half the periods of the structure to reduce the coupling between adjacent vertical microstrip lines without compromising the antenna performance in terms of scan range (see Section 2.3).

In this kind of antenna, the radiation sources can be represented by magnetic currents at the edge of the conductors [18, 19]. These currents are oppositely directed on the edges of the straight microstrip line sections, tending to cancel one another's radiation. In contrast, the magnetic current in the excess length created by a corner acts as the dominant radiation source. Nevertheless, the interconnecting microstrip lines introduce a phase shift between two consecutive radiators/bends. This phase shift, which depends on the line length and frequency, influences the variation in the main beam direction. The horizontal distances d and $d + l$ shown in Figure 1 define, for a given bandwidth, the main beam scan range. In contrast, the length a of the first and last horizontal segments connected with the feed or the matched load only influences the impedance matching of the antenna. The height h contributes to the phase shift between consecutive radiators, and W determinates the microstrip characteristic impedance for a given substrate height (h_{sub}) and permittivity (ε_r).

To investigate the effect of the geometric parameters, a numerical analysis of the two structures, shown in Figure 1, has been performed using the CST Studio Suite® inside a bandwidth of 1 GHz centred at 7.8 GHz. This range of frequencies was chosen because it respects the UWB indoor radio regulations in most countries worldwide [31, 32], resulting in a good solution for indoor UWB radar monitoring systems. Simulations were performed for a 1.524 mm thick Rogers RO4003C substrate [33]. Figure 2 reports a 3-D view of the rampart line antenna in the traditional geometry together with the adopted coordinate system.

FIGURE 2 3-D view of the rampart line antenna and adopted reference system

2.1 | Effect of unit cell trace length

The effect of the unit cell trace length ($2h + 2d + l$) on the far-field gain patterns was first investigated. Figure 3 shows the far-field cuts ($\phi = \pi/2$ in Figure 2) at 7.3 and 8.3 GHz. For simplicity, this analysis is carried out only for the configuration of Figure 1b. However, as will be shown in Section 2.2, an equivalent result can be obtained for the configuration of Figure 1a. Two antennas with 10 periods were designed. Both radiators have the same geometric parameters $W = 2$ mm, $a = 5.2$ mm, $d = 6.5$ mm. The value of l amounts to -3.5 mm for the first antenna (blue curves in Figure 3) and 2.5 mm for the second one (red curves in Figure 3). In addition, while $h = 18.2$ mm for the first configuration, it has been modified in the second structure to maintain the length $2h + 2d + l$ constant. Despite showing completely different scan ranges (53.3° and 35.4° for the first and the second design, respectively), the frequency at which the main beam is pointing towards broadside is approximately equal for both configurations. Furthermore, Figure 3 clearly shows that rampart line antennas vary the main beam direction with a varying feeding frequency.

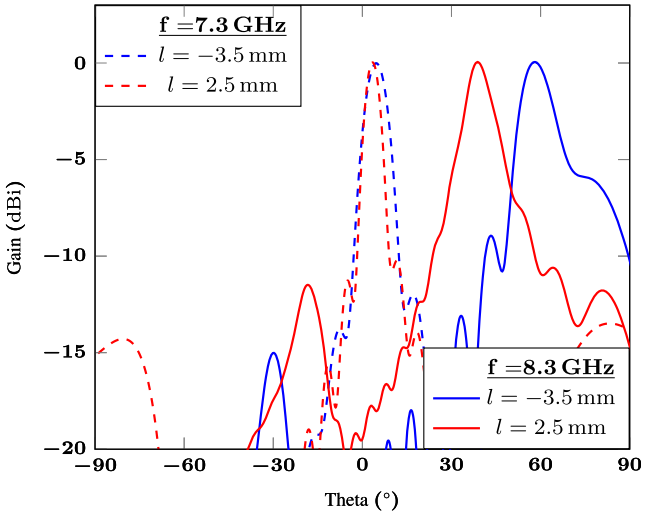

FIGURE 3 Effect of the total length of the unit cell on the far-field of the antenna

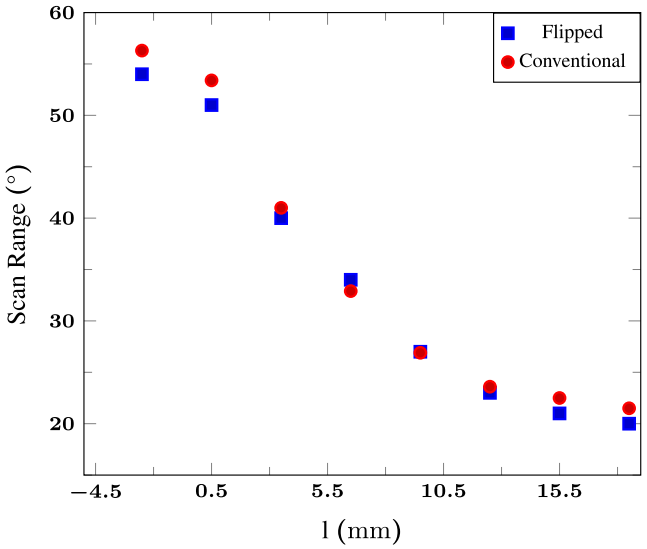

FIGURE 4 Scan range as a function of the distance between the radiators (horizontal direction) for $d = 5$ mm and l, varying from -2.5 to 18.5 mm

2.2 | Effect of horizontal distances

Figure 4 shows how variation in the horizontal distances (y direction) affects the scan range of the antenna, both for the conventional geometry and for the one with half the periods flipped. For all simulations, $d = 5$ mm and $W = 2$ mm, while h, equal to 19.2 mm at $l = -2.5$ mm, has been modified to maintain the total period length ($2(h + d) + l$). In Figure 4, it is clear that to increase the scan range, it is necessary to decrease the value of l, consequently reducing the distance between the vertically oriented microstrip lines. Furthermore, Figure 4 shows that the same geometric parameters provide the same scan range with a maximum discrepancy of 2.4° between the two geometries. This discrepancy increases for lower values of l, for which 2 consecutive periods are brought much closer. This can be explained by considering the difference in coupling between the considered geometries. Indeed, while for the geometry with half the periods flipped (Figure 1b), the coupling is mainly defined by the distance of the vertical microstrip lines inside the same unit cell, for the traditional geometry in Figure 1a, the lines belonging to the adjacent period also contribute to the coupling enhancement. Figure 5 instead represents the effect of the variation in d and l while keeping $2d + l$ constant. Simulations have been performed on the topology of Figure 1b, which achieved an identical scan range as the topology of Figure 1a with identical geometric parameters. Five different values for $2d + l$ have been considered (i.e. 5.5 mm, 9.5 mm, 13.5 mm, 21.5 mm, and 29.5 mm), W has been set equal to 2 mm, and h has been modified, starting from 20.2 mm at $l = -4.5$ mm and $d = 5$ mm, to maintain $2(h + d) + l$ constant. As can be seen in Figure 5, these configurations determine five scan ranges: 60°, 50°, 35°, 30°, and 20°. When $2d + l$ is kept constant, the scan range does not change by more than 2.4° for multiple combinations of d and l. This shows that with different horizontal length combinations, the same scan range can be obtained.

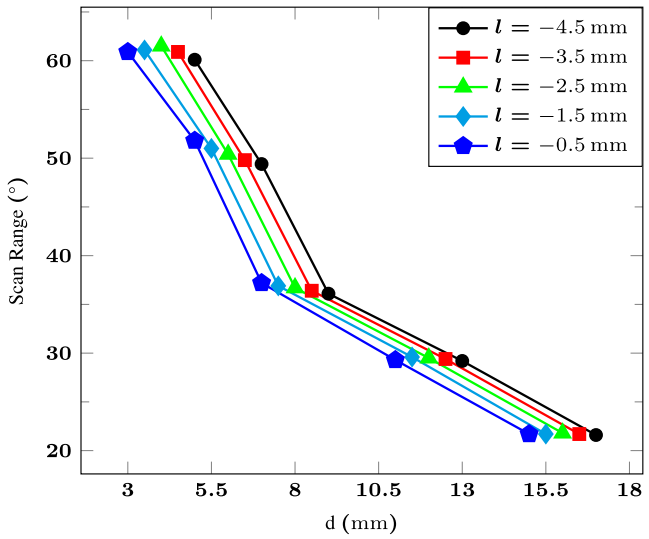

FIGURE 5 Scan range with various combinations of d and l while keeping $2d + l$ constant

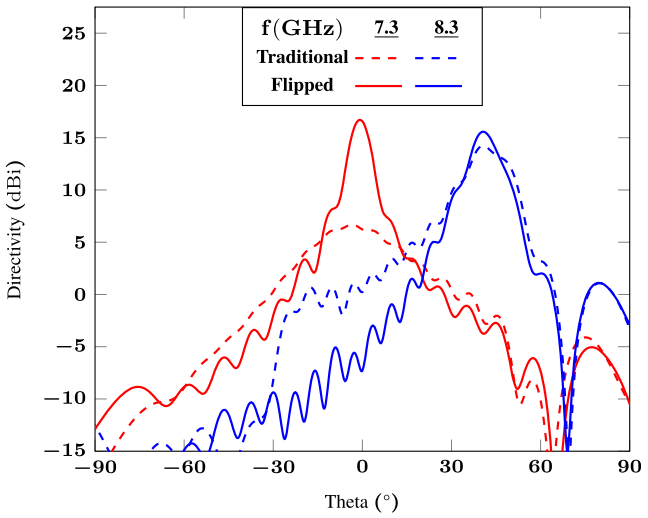

FIGURE 6 Directivity in the plane $\phi = \pi/2$ of two rampart line antennas with $a = 5.2$ mm, $W = 3.5$ mm, $l = -5$ mm, $d = 7$ mm, and $h = 15.1$ mm for the traditional (dashed lines) and proposed (solid lines) geometries

2.3 | Effect of coupling and proposed solution

As has been evidenced, reducing the horizontal distances leads to an increase in the scan range for a given bandwidth, but as a drawback, the vertical microstrip lines along the x-direction are brought closer to one another. If d or $d + l$ decreases too much, the coupling between the microstrip lines will no longer be negligible, which has nasty consequences for antenna performance. In particular, the reduced distance between vertical microstrip lines can be responsible for stronger resonances in the attenuation constant [28]. The effect on antenna performance is evident in Figure 6, which shows the far-field radiation pattern of two rampart line antennas with $a = 5.2$ mm, $W = 3.5$ mm, $l = -5$ mm, $d = 7$ mm, and $h = 15.1$ mm for the geometries of Figures 1a and 1b. In these configurations, $d + l = 2$ mm, representing a condition of elevated coupling. Because the two radiators have the same geometric parameters, the frequency at which the main beams are pointing towards broadside and the scan range are the same. However, while the beam direction is almost unchanged, the shape of the pattern is highly perturbed. For a wide scan range within a narrow frequency band, the horizontal distances between the radiators must be reduced, while multiple combinations of d and l can ensure the same scan range. For these particular cases, the best solution is to choose the proposed configuration of Figure 1b with $l = -d$ and the higher value of d to ensure the required scan range.

3 | THEORY AND MODELLING

According to the description in Section 2, the rampart line antenna can be modelled as an array of radiating sources. Each element can be represented as a magnetic dipole with the same direction as the corresponding diagonal chamfered corner. The total radiation pattern can then be obtained as the superposition of the dipoles' electric far-fields appropriately weighted in amplitude to account for the dielectric and metal losses of the interconnecting lines. Further, these are weighted in phase as a consequence of the geometric disposition of the bends and the phase shifts introduced by the interconnecting lines. Figure 7a represents the first 2 periods of the structure: the red arrows indicate the dipole directions, while the green dots identify the assumed phase centres required to calculate the phase shifts between two consecutive radiators. All the dipoles are projected along the y-axis, and the physical separation along the x-axis is ignored, allowing application of the array theory into its 1-D form [34]. The microstrip lines parallel to the x-axis with a length h are then only responsible for a phase shift between the radiators. The phase shift between two consecutive radiators is induced by the microstrip line interconnecting two consecutive green points in Figure 7a. It is assumed that higher-order modes are absent and that the effect of substrate surface waves is negligible. The new model will first be applied to the standard geometry (Figure 1a) and then extended to the other configuration, as shown in Figure 1b. The model in the present form is extremely versatile because it can be easily adapted to multiple meandered geometries (that could also differ from those described here). The model can be modified by only changing the orientations of the dipoles—representing the radiating sources—to describe various geometries.

As can be seen in Figure 7b, dipole 1 is rotated by an angle of $\alpha = 7\pi/4$, dipole 2 by an angle of $\alpha = 3\pi/4$, dipole 3 by an angle of $\alpha = \pi/4$, and dipole 4 by an angle of $\alpha = 5\pi/4$. The generic expression for the electric far-field when considering $\phi = \pi/2$ is

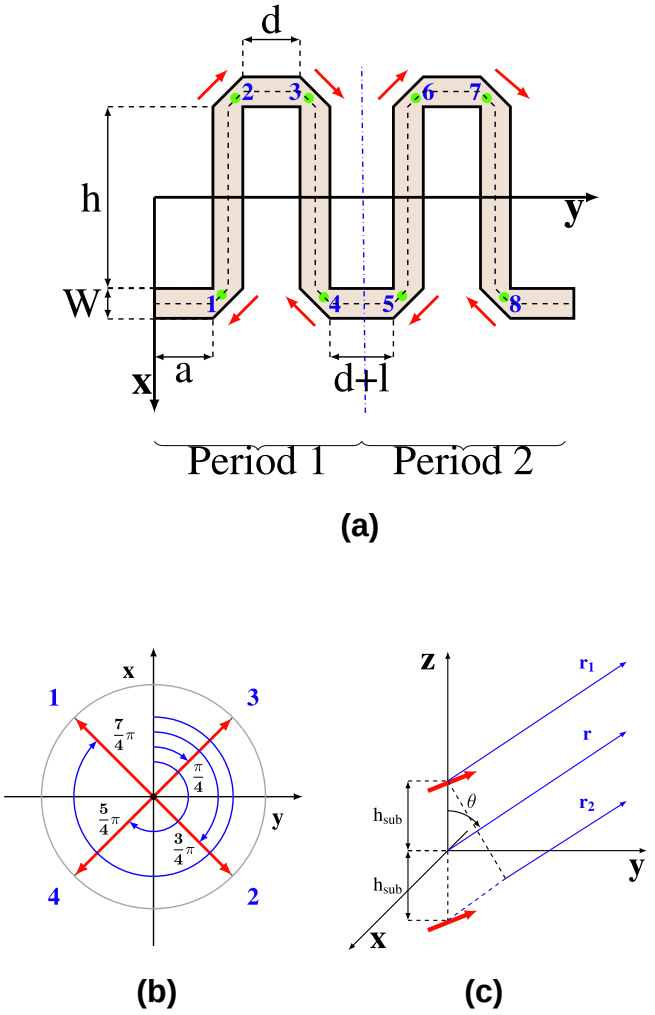

FIGURE 7 (a) Scheme for the antenna model, (b) angle of rotation α of the dipoles in 1 period (c) real magnetic dipole and its image

$$\boldsymbol{E}_{\text{tot}}(\theta) = \sum_{m=1}^{M} \boldsymbol{E}_{dm}(\theta) a_m e^{-j\delta_m} e^{jk_0 y_m \sin(\theta)} = \sum_{m=1}^{M} \boldsymbol{e}_m(\theta), \quad (1)$$

where M is the number of radiators, $E_m(\theta)$ is the electric field of the m_{th} magnetic dipole, k_0 is the free space propagation constant, a_m is the excitation amplitude, δ_m is the excitation phase, and y_m is the y coordinate of the m_{th} radiator considering the reference system in Figure 2. Both the total pattern and those of the individual elements are expressed as a function of the angles θ (see Figure 2). It is worth noting that the far electric field is not identical for all radiators but varies according to corner orientation.

In the following, all contributions of the total radiation pattern are analysed in more detail.

3.1 | Small magnetic dipole radiation pattern

To obtain the complete radiation patterns of the rampart antenna, it is necessary to know the radiation patterns of the single elements modelled as small magnetic dipoles. Considering the coordinate system reported in Figure 2, the electric vector potential $\boldsymbol{F}$ of this first element can be written as [30].

$$\boldsymbol{F} = \frac{I_m l_m \varepsilon_0}{4\pi r} e^{-jk_0 r} \cos(\alpha) \boldsymbol{u_x} + \frac{I_m l_m \varepsilon_0}{4\pi r} e^{-jk_0 r} \sin(\alpha) \boldsymbol{u_y}, \quad (2)$$

where $I_m l_m$ is the magnetic dipole moment, I_m is the magnetic current, $\varepsilon_0 = 8.854 \cdot 10^{-12}$, F/m is the free space permittivity, r is the radial distance, k_0 is the wave number in free space, and α is the dipole rotation angle. Using the vector potential, it is possible to compute the element electric far-fields $\boldsymbol{E}_m$ [30]. The expressions of the electric far-fields for the magnetic dipoles constituting the antenna for $\phi = \pi/2$ are given by

$$\boldsymbol{E}_{4m+1}(\theta) = -\boldsymbol{E}_{4m+2}(\theta) = \frac{j e^{-jk_0 r} I_m l_m k_0}{4\sqrt{2}\pi r} \boldsymbol{u}_\theta - \frac{j e^{-jk_0 r} I_m l_m k_0 \cos(\theta)}{4\sqrt{2}\pi r} \boldsymbol{u}_\phi, \quad m = 0, \ldots, M/4 - 1 \quad (3a)$$

$$\boldsymbol{E}_{4m+3}(\theta) = -\boldsymbol{E}_{4m+4}(\theta) = \frac{j e^{-jk_0 r} I_m l_m k_0}{4\sqrt{2}\pi r} \boldsymbol{u}_\theta + \frac{j e^{-jk_0 r} I_m l_m k_0 \cos(\theta)}{4\sqrt{2}\pi r} \boldsymbol{u}_\phi, \quad m = 0, \ldots, M/4 - 1. \quad (3b)$$

Because of the ground plane presence, it is, strictly speaking, necessary to consider each dipole's corresponding image source, although we have observed that the contributions may be ignored without serious consequences. For a magnetic dipole over a perfect electric conductor, the image source has the same direction as the original and is positioned at $z = -h_{\text{sub}}$, as represented in Figure 7c. Adding the contribution of the ground plane, the resulting electric vectors are

$$\boldsymbol{E}_{dm} = \boldsymbol{E}_m 2\cos(k_0 h_{\text{sub}} \cos(\theta)). \quad (4)$$

It is worth noting that the current model used for the elementary radiating source does not consider the effect of the substrate, which will only be included in the definition of the phase shift between two consecutive bends. This effect could be considered by replacing the elementary magnetic dipole with an aperture on the side of the microstrip bend, as detailed in [25]. However, this solution produces negligible variations in the 1-D antenna pattern and would then be responsible for increasing the model complexity without improving its accuracy.

3.2 | Contribution due to the physical distance between radiators

In the presented model, all the dipoles are projected along the y-axis to apply the 1-D array theory. The total electric field computation takes the physical distance between the radiators into account by means of the factor

$$e^{jk_0 y_m \sin(\theta)}, \tag{5}$$

where y_m is the y coordinate of the m_{th} radiator considering the reference system in Figure 7a.

3.3 | Element phase and amplitude excitation

The different dipoles are connected by microstrip lines that cause a phase shift and an attenuation of the excitation signal between two consecutive radiators, depending on the substrate properties. In general, the propagation constant of a microstrip line is given by

$$k_g = \beta_g - j\alpha_g, \tag{6}$$

where α_g and β_g are the attenuation and phase constants, respectively. The attenuation constant considers the losses in both the dielectric and the conductors [35]. The phase constant β_g is related to the guided wavelength λ_g as

$$\beta_g = \frac{2\pi}{\lambda_g} = \frac{2\pi}{\lambda_0}\sqrt{\varepsilon_{\text{eff}}(f)}, \tag{7}$$

where λ_0 is the free space wavelength, and $\varepsilon_{\text{eff}}(f)$ is the effective permittivity of the material due to the fringing field effect between strip and ground plane, which is computed at the considered frequency according to [36]:

$$\varepsilon_{\text{eff}}(f) = \left(\frac{\sqrt{\varepsilon_r} - \sqrt{\varepsilon_{\text{eff}}(0)}}{1 + 4F^{-1.5}} + \sqrt{\varepsilon_{\text{eff}}(0)}\right)^2, \tag{8}$$

where

$$F = \frac{4h_{\text{sub}}\sqrt{\varepsilon_r - 1}}{\lambda_0}\left(0.5 + \left(1 + 2\log\left(1 + \frac{W}{h_{\text{sub}}}\right)\right)^2\right). \tag{9}$$

The above equation gives the correct effective relative permittivity for the microstrip dimensions used to create Figure 9 and for the frequency range used (7.3–8.3 GHz). However, the beam direction is quite critical with respect to the correct value of the effective relative permittivity. In general, different equations need to be applied for different microstrip dimensions and frequency ranges [37].

For a proper rampart antenna design, we need to know which equation to apply before we set out to design the antenna. It appears that the effective relative permittivity values generated by the full-wave analysis program for a length of microstrip transmission line, using standard waveguide ports, lack sufficient accuracy for our needs.

To quickly generate the correct value for the effective relative permittivity, using the full-wave analysis software, we virtually replicate the measurement procedure of [38], adding SMA or at least coaxial connectors to the microstrip transmission line under test in our full-wave analysis program. We then analyse the scattering parameters for two lengths of transmission line, where we maximize the line length difference, as recommended in [38], while—at the same time—ensuring that the radiation is kept to a minimum.

The found values (as a function of frequency) from this simulated measurement can be used directly in the model, or—as we have done—can be compared with the equations listed in [37], after which the correct equation for use in the model is chosen.

Relating the equations in [37] to a wide set of microstrip dimensions, relative permittivities, and frequencies is the subject of an ongoing study.

The phase and amplitude variations between two consecutive elements due to the microstrip lines are given by

$$e^{-jk_g d_{\text{eff}}}, \tag{10}$$

where d_{eff} is the effective distance between the radiators. Contrary to what happens for the phase shift due to physical position, it is now necessary to consider an effective distance taking into account not only the line length but also the presence of the corners. In this work, two configurations have been considered: two radiators connected by a vertical microstrip line and two radiators connected by a horizontal microstrip line. The effective length is then computed as the geometric mean of the length of the centreline through the microstrip structure (blue lines in Figure 8) and of the shorter path connecting the starting and ending points of the centreline with the middle point of the bend (red line in Figure 8). For two radiators separated by a vertical line (Figure 8a), this results in

$$h_{\text{eff}} = \sqrt{\sqrt{\left(h + \frac{W}{2}\right)^2 + \left(\frac{W}{2}\right)^2}\left(h + \frac{W}{2}\sqrt{2}\right)}. \tag{11}$$

For two radiators separated by a horizontal line, the effective length is computed by

$$d_{\text{eff1, 2}} = \sqrt{2\sqrt{\left(\frac{d_{1,2}}{2} + \frac{W}{4}\right)^2 + \left(\frac{W}{4}\right)^2}\left(d_{1,2} + \frac{W}{2}\sqrt{2}\right)}, \tag{12}$$

where $d_1 = d$ and $d_2 = d + l$. Replacing the physical lengths by the effective lengths for the phase shift computation allows

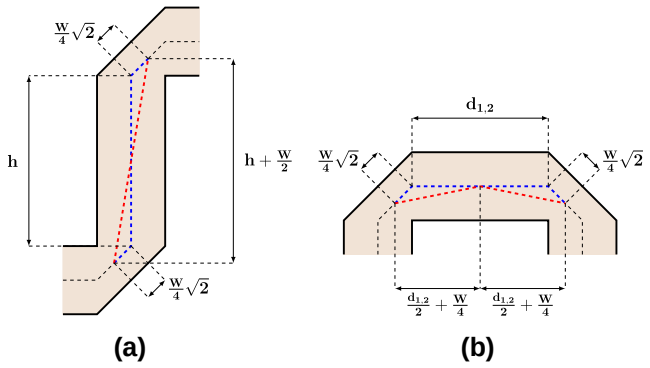

FIGURE 8 Path lengths for effective distance calculation between dipoles separated by (a) a vertical microstrip line and by (b) a horizontal microstrip line

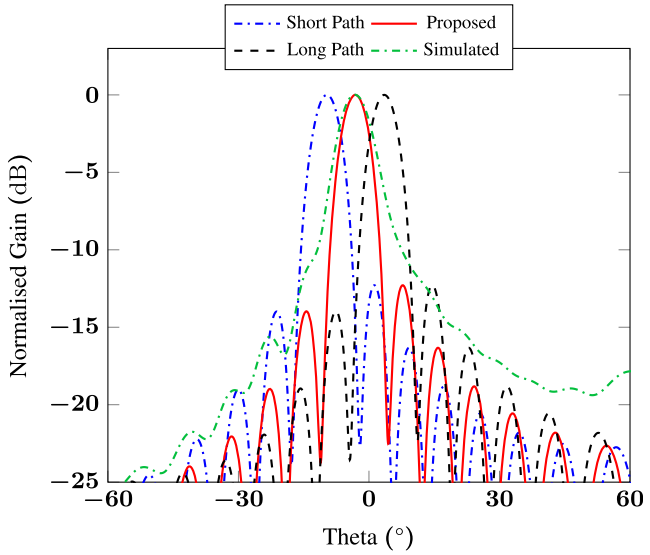

FIGURE 9 Effect of the bend correction on a rampart line antenna with the modified geometry designed on a substrate of Rogers RO4003C with $h_{sub} = 1.524$ mm, $a = 5.2$ mm, $W = 3.5$ mm, $l = -6.5$ mm, $d = 7$ mm, and $h = 14.2$ mm

better reconstruction of the effective distance between consecutive dipoles and better prediction of the main beam pointing direction. Figure 9 compares the far-field simulated by CST with the one computed by the model with and without length correction for the phase shift computation. Figure 9 shows the main beam direction obtained considering both the red and the blue paths of Figure 8. Without the correction, the main beam direction cannot be properly reconstructed and for both the longer and the shorter paths an error of about 6° is obtained. Clearly, it is fundamental to take into account the effective length of the bends to correctly reconstruct the main beam direction.

3.4 | Model formulation

Collecting all the contributions presented in Sections 3.2 and 3.3, it is possible to express the complete formulation of the model. For all dipoles in the array, an initial phase shift and loss are given by the microstrip feeding line. This contribution, being common to all the radiators, does not modify the main beam direction but rather influences only the return loss of the structure. This first term can be written as

$$e^{j\phi_0} = e^{-jk_g a_{eff}} e^{jk_0(a+W/4)\sin(\theta)}, \tag{13}$$

where a_{eff} is the effective length of the feeding line (Figure 1). Considering the first period, the contributions $\boldsymbol{e}_m(\theta), m = 1, 2, 3, 4$ of the first four dipoles are

$$\boldsymbol{e}_1(\theta) = \boldsymbol{E_{d1}}(\theta)e^{j\phi_0} \tag{14a}$$

$$\boldsymbol{e}_2(\theta) = -\boldsymbol{E_{d1}}(\theta)e^{j\phi_0}e^{jk_0 W/2\sin(\theta)}e^{-jk_g h_{eff}} \tag{14b}$$

$$\boldsymbol{e}_3(\theta) = -\boldsymbol{E_{d3}}(\theta)e^{j\phi_0}e^{jk_0(d+W)\sin(\theta)} \times e^{-jk_g(d_{eff1}+h_{eff})} \tag{14c}$$

$$\boldsymbol{e}_4(\theta) = \boldsymbol{E_{d3}}(\theta)e^{j\phi_0}e^{jk_0(d+3W/2)\sin(\theta)} \times e^{-jk_g(d_{eff1}+2h_{eff})}. \tag{14d}$$

Generalizing for an arbitrary number of unit cells N, the complete expression of the total electric far-field is

$$\boldsymbol{E}_{tot}(\theta) = \boldsymbol{e}_c(\theta)\sum_{n=0}^{N-1} e^{jk_0 2n(d+W+l/2)\sin(\theta)} \times e^{-jk_g n(d_{eff1}+d_{eff2}+2h_{eff})}, \tag{15}$$

where

$$\boldsymbol{e}_c(\theta) = e^{j\phi_0}\Big(\boldsymbol{E_{d1}}(\theta) + \boldsymbol{E_{d3}}(\theta)e^{jk_0(d+W)\sin(\theta)} \times e^{-jk_g(h_{eff}+d_{eff1})}\Big)\left(1 - e^{jk_0 W/2\sin(\theta)}e^{-jk_g h_{eff}}\right). \tag{16}$$

The result of Equation (15) can be easily modified to the geometry of Figure 1b, considering that in the flipped periods, the electric field θ component is the same as the one computed for the geometry of Figure 1a, while the ϕ component is the opposite.

4 | SIMULATION RESULTS

To validate the presented model, full-wave simulation results were compared with the predictions made using the equations in Section 3. The structures represented in this section have not been optimized in terms of performances and are only used to verify the ability of the model to predict the effective main beam pointing direction. The simulations results refer to the geometry of Figure 1b with the same scan range of the one in Figure 1a without the inconvenience of

the coupling. Simulations were performed considering three different materials, being Rogers RT/duroid 6202 ($\varepsilon_r = 2.90$ and $\tan\delta = 0.0015$ at 10 GHz) [39], Rogers RO4003C ($\varepsilon_r = 3.55$, $\tan\delta = 0.0027$ at 10 GHz) [33], and Rogers RT/duroid 6006 ($\varepsilon_r = 6.45$, $\tan\delta = 0.0027$ at 10 GHz) [40]. For each substrate material, a rampart line antenna working in the band of 7.3 to 8.3 GHz was designed. To verify the accuracy of the model for different substrate thicknesses, simulations with the Rogers RT/duroid 6202 substrate, obtained by means of the proposed model and full-wave simulations, were performed for a substrate thickness of $h_{\text{sub}} = 0.762$ mm, on RT/duroid 6006 substrate for a substrate thickness of $h_{\text{sub}} = 0.254$ mm, and on Rogers RO4300C for a substrate thickness of $h_{\text{sub}} = 1.524$ mm. The normalized far-field gain patterns for the structures designed employing the Rogers RT/duroid 6202, Rogers RO4003C, and Rogers RT/duroid 6006 are shown in Figures 10, 11, and 12. The dimensions of the different antenna designs are listed in the captions of the corresponding figures. For all tested configurations, substrate thickness, and permittivity, the model results are in close agreement with full-wave simulations, with a maximum error of about 2°.

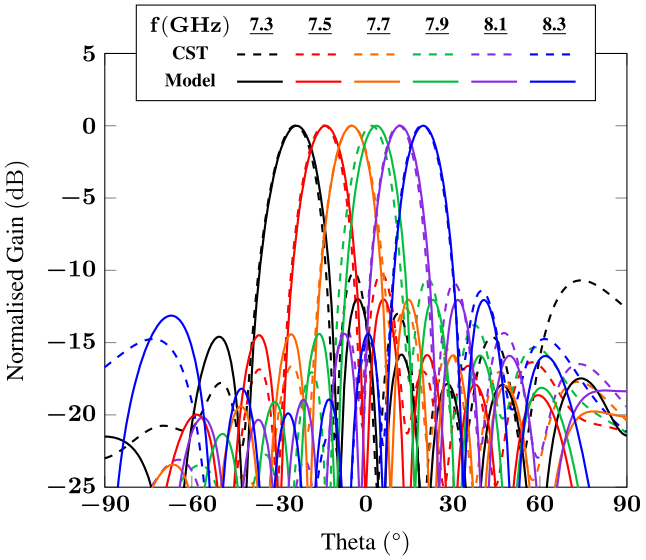

FIGURE 10 Main beam pointing directions of a rampart line antenna with the geometry of Figure 1b designed on a substrate of RT duroid 6202 ($\varepsilon_r = 2.90$ and $\tan\delta = 0.0015$ at 10 GHz), with $h_{\text{sub}} = 0.762$ mm, $a = 5.2$ mm, $W = 3.5$ mm, $l = -5.5$ mm, $d = 6$ mm, and $h = 16.5$ mm

5 | PROTOTYPE REALIZATION AND MEASUREMENTS

A prototype of the rampart line antenna was realized on a Rogers RO4350B substrate [33] with a 1.524 mm thickness. The selected configuration is the one with half the periods flipped as shown in Figure 1b. The optimized antenna dimensions are $d = -l = 5$ mm, $W = 3.5$ mm, and $h = 16.5$ mm. The antenna is designed to support a scan range of about 60° in a bandwidth of 1 GHz at a central frequency of 7.8 GHz. To further reduce the coupling, l has been chosen equal to $-d$, thus allowing selection of the largest value of d that can assure the required scan range. Figure 13 compares the radiation patterns in the $\phi = \pi/2$ plane obtained with CST with those calculated with the proposed model. As can be seen, the model results are in agreement with the full-wave simulations, and the maximum error in the beam direction estimation amounts to 2.8° at 8.3 GHz for a 3 dB beamwidth of 16.9°. In addition, the prototype was characterized while deployed inside an anechoic chamber. A comparison between the simulated and measured antenna reflection coefficient is reported in Figure 14. Radiation pattern measurements were performed in the anechoic chamber using an Orbit/FR antenna positioning system with the set-up shown in Figure 15. The far-field gain pattern of the antenna under test (AUT), being the rampart line antenna prototype, is retrieved by means of a gain transfer procedure [41]. First, a free space far-field link was set up between the AUT and a UWB horn (R&S HF906 oriented towards the AUT) with their phase centres separated by 4.60 m. Using a calibrated Keysight N5242 B PNA-X vector network analyser and the antenna positioning system, the two-port scattering parameters for various orientations of the AUT are measured for both horizontal and vertical polarizations of the UWB

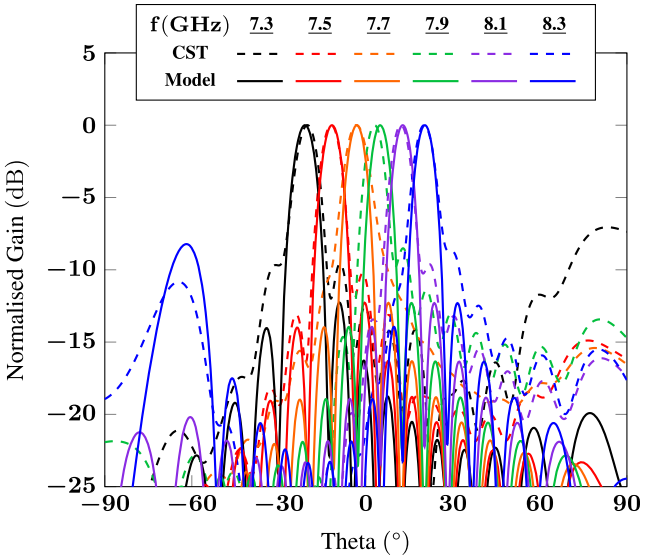

FIGURE 11 Main beam pointing directions of a rampart line antenna with the geometry of Figure 1b designed on a substrate of Rogers RO4003C ($\varepsilon_r = 3.55$, $\tan\delta = 0.0027$ at 10 GHz), with $h_{\text{sub}} = 1.524$ mm, $a = 5.2$ mm, $W = 3.5$ mm, $l = -6.5$ mm, $d = 7$ mm, and $h = 14.2$ mm

horn, yielding the uncalibrated gain pattern of the AUT. Subsequently, the rampart line antenna prototype is replaced by a standard gain horn (MI-12-5.8 and MI-12-8.2 [42]) such that its phase centre is at the same position. By measuring the two-port scattering parameters for a few well-chosen orientations of the standard gain horn, the gain pattern of the AUT obtained in the first step can now be calibrated, as the gain of the horn is now accurately known. The calibrated far-field gain patterns of the rampart line antenna in the upper-half-space ($\theta \leq 90°$, see Figure 2) from 7.3 to 8.3 GHz are shown in

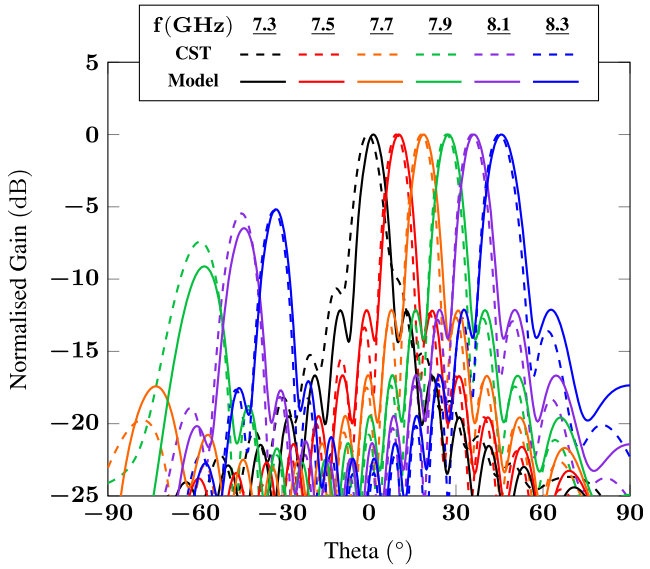

FIGURE 12 Main beam pointing directions of a rampart line antenna with the geometry of Figure 1b designed on a substrate of Rogers RT/duroid 6006 ($\varepsilon_r = 6.45$, $\tan\delta = 0.0027$ at 10 GHz), with $h_{sub} = 0.254$ mm, $a = 5.2$ mm, $W = 0.5$ mm, $l = 0.5$ mm, $d = 6.5$ mm, and $h = 11.5$ mm

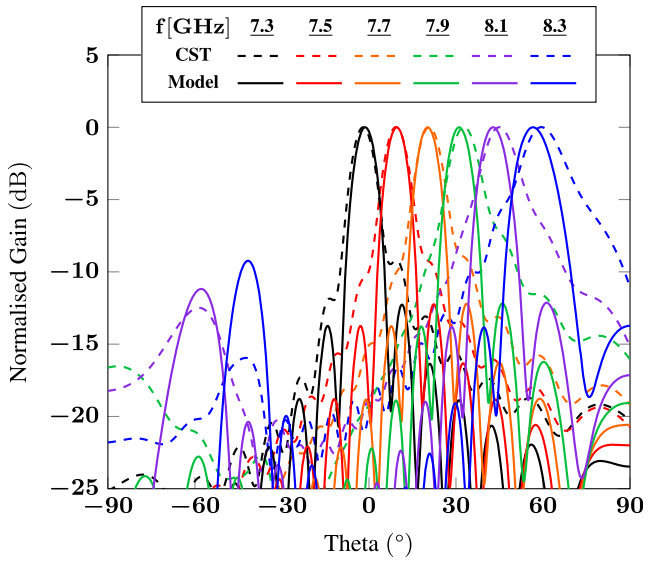

FIGURE 13 Simulated and computed normalized gain of the realized rampart line antenna

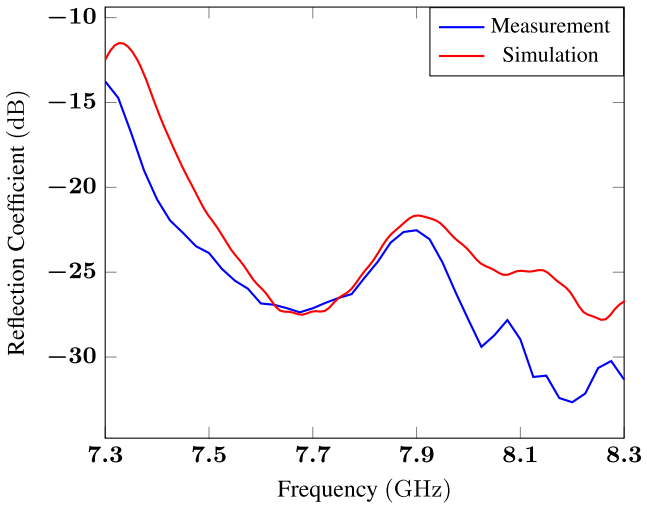

FIGURE 14 Simulated and measured reflection coefficient of the realized rampart line antenna

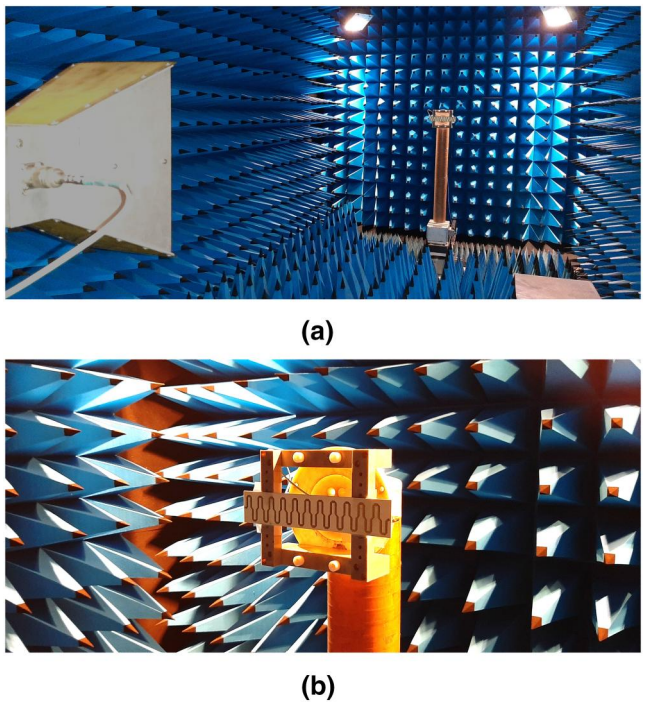

FIGURE 15 Photo of (a) complete set-up and (b) designed antenna prototype on a dielectric easel

Figures 16 and 17. A good agreement can be noticed between simulations and measurements with a minor discrepancy around $\theta = 90°$. This may be attributed to the fact that simulations did not consider the presence of the feeding cable. Figure 18 represents instead the simulated and measured antenna gain and main beam direction as a function of the frequency. While measured data refer only to the antenna operating band (7.3–8.3 GHz [1]), the simulated points also report the value inside the range 6.9–7.2 GHz to show the antenna behaviour while the beam is pointing towards broadside. This kind of antenna is known for the open stop band effect that is responsible for suppressing radiation at broadside. This phenomenon can be described from a LWA point of view through the use of the Bloch-Floquet theorem [26, 28, 29, 43, 44], but also from a PAA point of view. In the latter, small reflections from the radiating elements and the phase shifters will add in phase at the broadside frequency and create a backward wave, causing a high attenuation [21]. As it is possible to see, with the proposed solution the antenna gain remains reasonably constant while the beam points towards broadside. At 7.3 GHz, the gain reduction is about 1 dBi.

6 | CONCLUSION

This work focuses on rampart line antennas as a compact and low-cost solution for applications requiring frequency-steering of the main beam direction. An analytical model based on 1-D array theory was proposed. The radiation sources are associated with the bends and represented by magnetic dipoles with the same orientation as the corners, while interconnecting microstrip lines determine the phase shifts and attenuations between these radiators. Contrary to previously proposed models, the effective distance between two radiators is computed by taking the equivalent length of the bends into account instead of their physical distance. Furthermore, the proposed model can be easily adapted to different antenna configurations by solely modifying the dipole orientation according to the disposition of the corners. The model has been tested for several substrate relative permittivity values ranging from 2.9 to 6.45. An alternative geometry has been proposed that is obtained by flipping half the periods of the structure around the y-axis in Figure 2. Using this solution, the coupling is influenced only by the microstrip lines in the x-direction belonging to the same periods and not those of the adjacent periods. Therefore, this configuration provides a solution when wide scan ranges in narrow frequency bands are required, for which the distance between the x-direction-oriented antenna lines must be drastically reduced. A prototype of the antenna with the proposed geometry has been realized and characterized, validating its performance. Both the reflection coefficient as a function of frequency and the far-field radiation patterns at multiple frequencies were measured. The computation time of the model implemented in software is orders of magnitude smaller than a run with a full-wave analysis program, making design optimization easier.

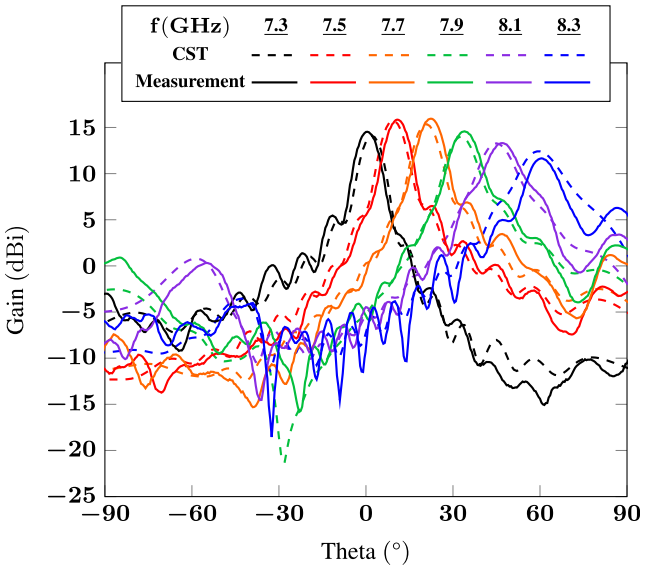

FIGURE 16 Simulated and measured gain of the realized rampart line antenna

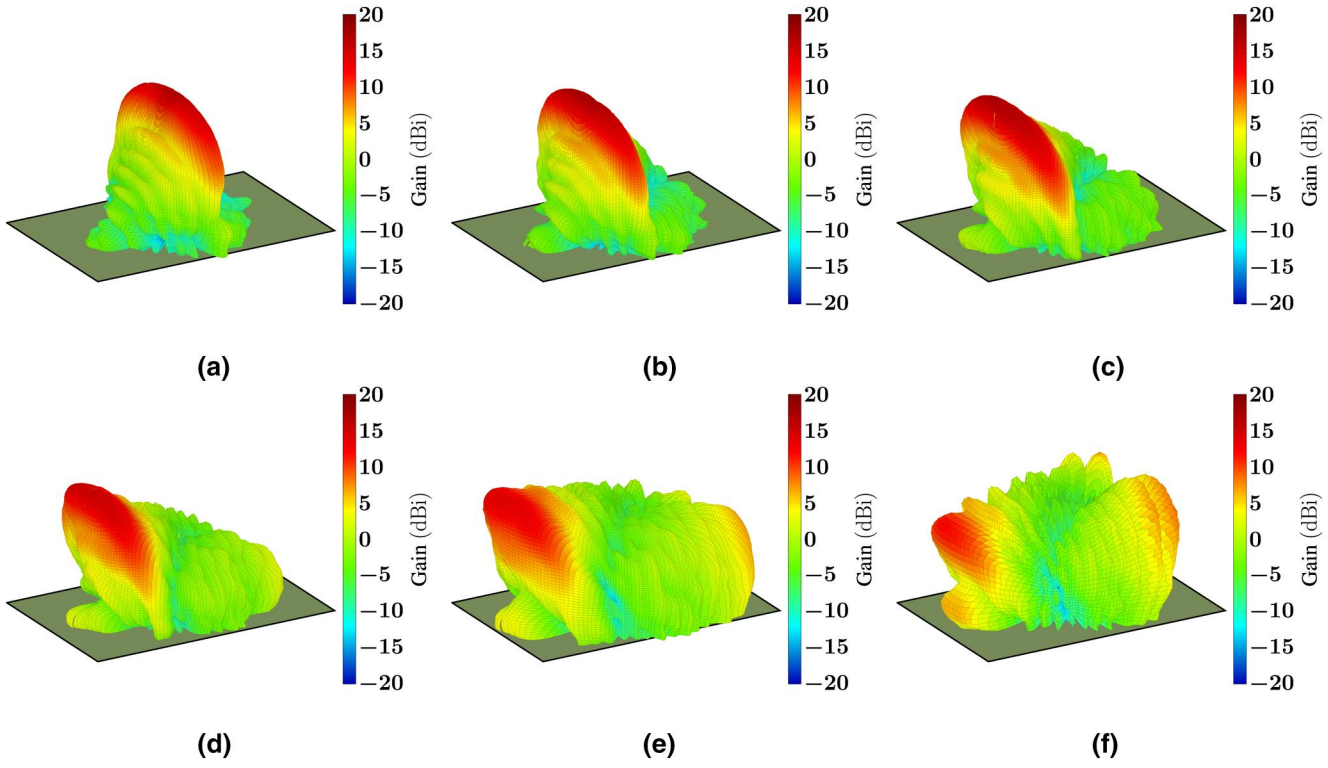

FIGURE 17 3-D gain measurement in the upper-half-space at (a) 7.3 GHz, (b) 7.5 GHz, (c) 7.7 GHz, (d) 7.9 GHz, (e) 8.1 GHz, and (f) 8.3 GHz

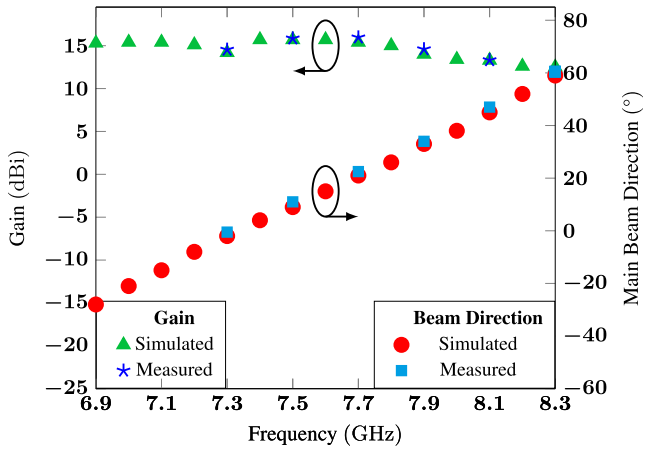

FIGURE 18 Simulated and measured gain and main beam direction as a function of the frequency

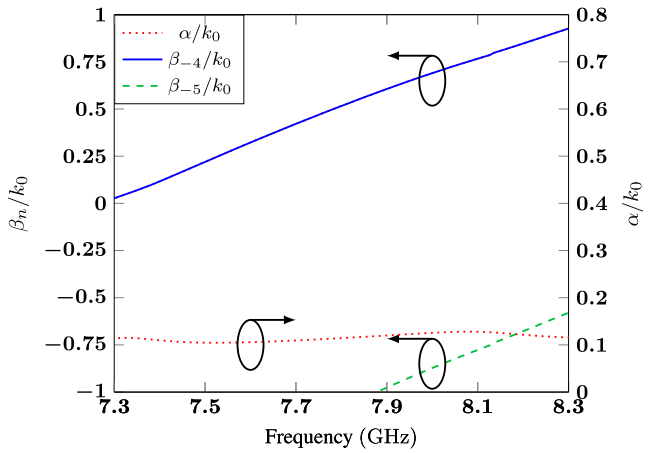

FIGURE 19 Phase and attenuation constants of the realized antenna as a function of frequency

ACKNOWLEDGEMENT

The authors wish to thank S. Lemey and H. Rogier, both from IDLab, Ghent University, for the fruitful discussions concerning image sources and effective relative permittivity, and D. Comite from Sapienza University of Rome and W. Fuscaldo from the Italian National Research Council for help with the leaky-wave antenna model.

ORCID

Giulia Sacco https://orcid.org/0000-0002-3663-9784

REFERENCES

1. Mercuri, M., et al.: 2-D localization, angular separation and vital signs monitoring using a SISO FMCW radar for smart long-term health monitoring environments. IEEE Internet Things J 1–1 (2021)
2. Schneider, D.A., et al.: A low-loss W-band frequency-scanning antenna for wideband multichannel radar applications. IEEE Antenn Wireless Propag Lett. 18(4), 5 (2019)
3. Boskovic, N., Jokanovic, B., Radovanovic, M.: Printed frequency scanning antenna arrays with enhanced frequency sensitivity and sidelobe suppression. IEEE Trans Antenn Propag. 65(4), 1757–1764 (2017)
4. Cao, W., et al.: Gain enhancement of beam scanning substrate integrated waveguide slot array antennas using a phase-correcting grating cover. IEEE Trans Antenn Propag. 62(9), 4584–4591 (2014)
5. Gentile, G., et al.: Silicon-filled rectangular waveguides and frequency scanning antennas for mm-wave integrated systems. IEEE Trans Antenn Propag. 61(12), 5893–5901 (2013)
6. Xu, J.F., et al.: Design and implementation of low sidelobe substrate integrated waveguide longitudinal slot array antennas. IET Microw, Antennas Propag. 3(5), 790 (2009)
7. Peng, Z.: A portable K-band 3-D MIMO radar with nonuniformly spaced array for short-range localization. IEEE Trans Microw Theor Tech. 66(11), 12 (2018)
8. Feger, R., et al.: A 77-GHz FMCW MIMO radar based on an SiGe single-chip transceiver. IEEE Trans Microw Theor Tech. 57(5), 1020–1035 (2009)
9. Vasanelli, C., Waldschmidt, C.: Assessment of a millimetre-wave antenna system for MIMO radar applications. IEEE Antenn Wireless Propag Lett. 16, 4 (2017)
10. Improvements or relating to high frequency electrical conductors or radiators. British patent no. 515684
11. Moradian, M., Tayarani, M., Khalaj-Amirhosseini, M.: Planar slotted array antenna fed by single wiggly-ridge waveguide. IEEE Antenn Wireless Propag Lett. 10, 764–767 (2011)
12. Mbaye, M., et al.: Bandwidth broadening of dual-slot antenna using substrate integrated waveguide (SIW). IEEE Antenn Wireless Propag Lett. 12, 1169–1171 (2013)
13. Bauer, F., Menzel, W.: A 79-GHz resonant laminated waveguide slotted array antenna using novel shaped slots in LTCC. IEEE Antenn Wireless Propag Lett. 12, 296–299 (2013)
14. Nicholson, K.J., et al.: Coaxial right/left-handed transmission line for electronic beam steering in the slotted waveguide antenna stiffened structure. IEEE Trans Microw Theor Tech. 62(4), 6 (2014)
15. Ghasemi, A., Laurin, J.J.: Beam steering in narrow-wall slotted ridge waveguide antenna using a rotating dielectric slab. IEEE Antenn Wireless Propag Lett. 17(10), 1773–1777 (2018)
16. Coetzee, J.C., Sheel, S.: Waveguide slot array design with compensation for higher order mode coupling between inclined coupling slots and neighbouring radiating slots. IEEE Trans Antenn Propag. 67(1), 12 (2019)
17. Lu, J., et al.: Broadband dual-polarized waveguide slot filtenna array with low cross polarization and high efficiency. IEEE Trans Antenn Propag. 67(1), 151–159 (2019)
18. Hall, P.S.: Microstrip linear array for polarisation-agile antenna applications. In: 11th European Microwave Conference, 1981, pp. 813–818. Amsterdam: IEEE (1981)
19. Hall, P.S.: Microstrip linear array with polarisation control. IEE Proc H Microw Opt Antenn. 130(3), 215 (1983)
20. Nishimura, S., Nakano, K., Makimoto, T. Franklin type microstrip line antenna. In: 1979 Antennas and Propagation Society International Symposium. 17. IEEE, pp. 134–137. (1979)
21. Henriksson, J., Markus, K., Tiuri, M.: A circularly polarized Travelling-wave Chain antenna. In: 9th European Microwave Conference, pp. 174–178. Brighton: IEEE (1979)
22. Chen, S.Y., Hsu, P.: Open-ended rampart slot array antenna fed by a CPW. IEEE Antenn Wireless Propag Lett. 4, 3 (2005)
23. Chen, S.Y., Lan, I.C., Hsu, P.: In-line series-feed collinear slot array fed by a coplanar waveguide. IEEE Trans Antenn Propag. 55(6), 1739–1744 (2007)
24. Calla, O.P.N., et al.: Empirical relation for designing the meander line antenna. In: 2008 International Conference on recent Advances in Microwave theory and applications, pp. 695–697. Jaipur, Rajasthan: IEEE (2008)
25. Patra, K., Dhar, S., Gupta, B.: Transmission line model for analysis of microstrip travelling wave antennas with right angled bends. AEU – Int J Electron Commun. 84, 375–386 (2018)
26. Cheng, S., et al.: An approximate circuit model to analyse microstrip rampart line in OSB suppressing. IEEE Access. 7, 90412–90417 (2019)

27. Nakano, H., et al.: Analysis and measurements for improved crank-line antennas. IEEE Trans Antenn Propag. 45(7), 7 (1997)
28. Ahmed, Z., et al.: Investigation of frequency scanning printed Bruce array antenna. IEEE Access. 8, 189003–189012 (2020)
29. Ahmed, Z., McEvoy, P., Ammann, M.J.: A wide frequency scanning printed bruce array antenna with bowtie and semi-circular elements. Sensors. 20(23), 6796 (2020)
30. Balanis, C.A.: Antenna theory: analysis and design, 3rd ed. John Wiley, Hoboken, NJ (2005)
31. European Telecommunications Standards Institute (ETSI): Short Range Devices (SRD) Using Ultra Wide Band Technology (UWB); Harmonised Standard Covering Essential Requirements of Article 3.2 of the Directive 2014/53/EU; Part 1: Requirements for Generic UWB Applications (2016). https://www.etsi.org/deliver/etsi\text{_}en/302000\text{_}302099/30206501/02.01.00\text{_}20/en\text{_}30206501v020100a.pdf
32. Electronic Code of Federal Regulation: Title 47: Telecommunication https://www.ecfr.gov/cgi-bin/text-idx?SID=cd32a47912c0c77ab28888fc828fb91f&mc=true&node=pt47.1.15&rgn=div5#se47.1.15\text{_}1517
33. Rogers Corporation: RO4000® Series High Frequency Circuit Materials (2018). https://rogerscorp.com/-/media/project/rogerscorp/documents/advanced-connectivity-solutions/english/data-sheets/ro4000-laminates-ro4003c-and-ro4350b---data-sheet.pdf
34. Visser, H.J.: Array and Phased Array Antenna Basics: Visser/Array and Phased Array Antenna Basics. Chichester: John Wiley & Sons, Ltd (2005)
35. Pozar, D.M.: Microwave Engineering, 4th ed. John wiley & sons (2011)
36. Yamashita, E., Atsuki, K.: An approximate dispersion formula of microstrip lines for computer aided design of microwave integrated circuits. MTT-S International Microwave Symposium Digest, vol. 79, pp. 320–322, Orlando: MTT005 (1979)
37. Sadiku, M.N.O., Musa, S.M., Rao Nelatury, S.: Comparison of dispersion formulas for microstrip lines. In: IEEE SoutheastCon, 2004. Proceedings. pp. 378–382. Greensboro, NC: IEEE (2004)
38. Das, N.K., Voda, S.M., Pozar, D.M.: Two methods for the measurement of substrate dielectric constant. IEEE Trans Microw Theor Tech. 35(7), 636–642 (1987)
39. Rogers Corporation: RT/duroid® 6202 High Frequency Laminates (2019). https://rogerscorp.com/-/media/project/rogerscorp/documents/advanced-connectivity-solutions/english/data-sheets/rt-duroid-6202-laminate-data-sheet.pdf
40. Rogers Corporation: RT/duroid® 6006/6010LM High Frequency Laminates (2017). https://rogerscorp.com/-/media/project/rogerscorp/documents/advanced-connectivity-solutions/english/data-sheets/rt-duroid-6006-6010lm-laminate-data-sheet.pdf
41. Hollis, J.S., Lyon, T.J., Clayton, L.: Microwave Antenna Measurements, 3rd ed. United States of America (1969)
42. MI Technologies: MI-12 Series Standard Gain Horns (2012). https://nscainc.com/wp-content/uploads/pdf/SA\text{_}12-12.pdf
43. Memarian, M., Eleftheriades, G.V.: Dirac leaky-wave antennas for continuous beam scanning from photonic crystals. Nat Commun. 6(1), 5855 (2015)
44. Jackson, D.R., Caloz, C., Itoh, T.: Leaky-wave antennas. Proc IEEE. 100(7), 2194–2206 (2012)
45. Lyu, Y.L., et al.: Periodic SIW leaky-wave antenna with large circularly polarized beam scanning range. IEEE Antenn Wireless Propag Lett. 16, 2493–2496 (2017)
46. Otto, S.: Solution to the broadside Problem and Symmetry Properties of periodic leaky-wave antennas [PhD Thesis]. Duisburg-Essen University (2016). https://core.ac.uk/download/pdf/44685548.pdf
47. Oliner, A.: Leaky wave antennas, chapter 5. In: Johnson, R.C. (ed.) Antena Engineering Handbook, 3rd ed. McGraw-Hill (1993)
48. Fuscaldo, W., Jackson, D.R., Galli, A.: A general and accurate formula for the beamwidth of 1-D leaky-wave antennas. IEEE Trans Antenn Propag. 65(4), 1670–1679 (2017)
49. Fuscaldo, W., Jackson, D.R., Galli, A.: New Beamwidth formulas for 1-D leaky-wave antennas: a review. In: 2019 PhotonIcs & electromagnetics Research Symposium – Spring (PIERS-Spring), pp. 9. IEEE, Rome (2019)

How to cite this article: Sacco, G., et al.: Analysis and modelling of rampart line antennas. IET Microw. Antennas Propag. 15(12), 1605–1617 (2021). https://doi.org/10.1049/mia2.12168

APPENDIX

Rampart line antennas can be studied with the leaky-wave antenna approach. More specifically, the wave numbers associated to the antenna spatial modes can be obtained from

$$\cosh\left(jk_{g,0}P\right) = \frac{A+D}{2}, \tag{17}$$

where $P = 2d + l + 2W$ is the period of the structure, and A and D are the elements of the ABCD matrix of the unit cell obtained from the scattering parameters with conventional conversion formulae [35]. According to the Bloch–Floquet theorem, the wave numbers of space harmonics that can be excited in a LWA can be expressed as [45–47].

$$k_{g,n} = k_{g,0} + \frac{2\pi n}{P}, \quad n = 0, \pm 1\ldots, \tag{18}$$

with n being an integer. The phase and the attenuation constants of the designed structure inside the antenna operating band are reported in Figure 19. It is possible to see that no strong variation in the attenuation constant appears while the beam is pointing towards broadside (7.3 GHz), thus confirming the results of Figure 18, where only a moderate gain reduction can be observed at this

TABLE 1 Absolute error in the main beam pointing direction and 3 dB beamwidth with the proposed model (PAA) and the leaky-wave antenna (LWA) model

	$\Delta\theta_m$ (°)		$\Delta\theta_{3dB}$ (°)	
Frequency (GHz)	**PAA**	**LWA**	**PAA**	**LWA**
7.3	0.69	2.26	0.57	1.89
7.5	0.29	1.66	1.26	2.89
7.7	0.52	0.68	1.43	2.78
7.9	1.60	0.73	2.35	3.07
8.1	2.12	0.74	3.67	3.86
8.3	2.81	1.45	4.01	6.03

Abbreviations: LWA, leaky-wave antenna; PAA, phased array antenna.

frequency. The main beam pointing direction can be computed considering

$$\sin(\theta_m) = \frac{\beta_{g,n}}{k_0}, \tag{19}$$

while the main 3 dB beamwidth results from [48, 49].

$$\theta_{3dB} = \theta_m - arcsin\left(\beta_{g,n}/k_0 - t_h(A_n)/L_n\right), \tag{20}$$

where $L_n = k_0 PN/2$, $A_n = \alpha/k_0 L_n$, and

$$t_h(A_n) = 1.3915\left(1 - tanh\left(q_1 A_n\right)\right) + A_n \, tanh\left(p_1 A_n\right) \tag{21}$$

with $q_1 = 0.021$ and $p_1 = 0.21$. Table 1 shows the absolute value of the error in the main beam pointing direction ($\Delta\theta_m$) and in the 3 dB beamwidth ($\Delta\theta_{3dB}$) obtained comparing the CST results with the one proposed and the LWA model. It can be seen that the proposed model results are comparable to those obtained with the LWA formulation, with the advantage that with our model, the solution can be obtained solely with knowledge of the geometric parameters without requiring simulation of the unit cell.